











Dipolar and quadrupolar correlations in the $5d^2$ Re-based double perovskites Ba_2YReO_6 and $\text{Ba}_2\text{ScReO}_6$

Otkur Omar ¹, Yang Zhang ², Qiang Zhang ³, Wei Tian ³, Elbio Dagotto ^{2,4}, Gang Chen ⁵, Taka-hisa Arima ^{6,7},
Matthew B. Stone ³, Andrew D. Christianson ⁴, Daigorou Hirai ^{8,9,*} and Shang Gao ^{1,3,4,†}

¹*Department of Physics, University of Science and Technology of China, Hefei, Anhui 230026, China*

²*Department of Physics and Astronomy, University of Tennessee, Knoxville, Tennessee 37996, USA*

³*Neutron Scattering Division, Oak Ridge National Laboratory, Oak Ridge, Tennessee 37831, USA*

⁴*Materials Science and Technology Division, Oak Ridge National Laboratory, Oak Ridge, Tennessee 37831, USA*

⁵*International Center for Quantum Materials, School of Physics, Peking University, Beijing 100871, China*

⁶*RIKEN Center for Emergent Matter Science, Wako, Saitama 351-0198, Japan*

⁷*Department of Advanced Materials Science, University of Tokyo, Kashiwa, Chiba 277-8561, Japan*

⁸*Department of Applied Physics, Nagoya University, Nagoya, Aichi 464-8603, Japan*

⁹*Institute of Solid State Physics, University of Tokyo, Kashiwa, Chiba 277-8581, Japan*



(Received 6 February 2025; revised 11 June 2025; accepted 1 July 2025; published 4 August 2025)

Double perovskites containing heavy transition-metal ions are an important family of compounds for the study of the interplay between electron correlation and spin-orbit coupling. Here, by combining magnetic susceptibility, heat capacity, and neutron scattering measurements, we investigate the dipolar and quadrupolar correlations in two prototypal rhenium-based double perovskite compounds Ba_2YReO_6 and $\text{Ba}_2\text{ScReO}_6$. A type-I dipolar antiferromagnetic ground state with a propagation vector $\mathbf{q} = (0, 0, 1)$ is observed in both compounds. At temperatures above the magnetic transitions, a quadrupolar ordered phase is identified. Weak spin excitations, which are gapped at low temperatures and softened in the correlated paramagnetic phase, are explained using a minimal model that considers both the dipolar and quadrupolar interactions. At larger wave vectors, we observe dominant phonon excitations that are well described by density functional calculations.

DOI: [10.1103/gwph-w9zm](https://doi.org/10.1103/gwph-w9zm)

I. INTRODUCTION

Electron correlations and spin-orbit coupling (SOC) are two essential ingredients to achieve exotic states in condensed matter. In compounds consisting of the $4d$ or $5d$ heavy transition-metal ions, the interplay between these two ingredients may lead to even richer phenomena [1–3]. For instance, in Sr_2IrO_4 , SOC entangles the spin and orbital degrees of freedom of the Ir^{4+} ($5d^5$) ions, resulting in a Mott-insulating ground state formed by effective angular momentum electron bands [4,5]. In $\alpha\text{-RuCl}_3$ that is composed of the magnetic Ru^{3+} ($4d^5$) ions, SOC-driven anisotropic interactions may induce a Kitaev quantum spin liquid, which holds great promise for applications in quantum computation [6–9].

The $5d$ -based double perovskites (DPs), with a chemical formula of $A_2BB'O_6$, are exemplary platforms for the study of the interplay between electron correlations and SOC [10]. In these materials, the B' sites, being occupied by the $5d$ heavy transition-metal ions, form a face-centered-cubic lattice as shown in Fig. 1. Figure 2 describes the typical energy levels of the $5d^2$ heavy transition-metal ions in the DPs. In these compounds, the d electron orbitals with angular momentum $L = 2$ are split into a t_{2g} ground-state triplet and an e_g excited-state doublet due to a strong crystal electric field. The t_{2g} ground

state, which can be described as orbitals of an effective angular momentum $\tilde{l} = 1$, is further coupled to the spin degree of freedom through SOC. This leads to a ground-state manifold that is described by an effective total angular momentum J_{eff} . The energy splitting for the heavy transition-metal ions in the DPs can be understood in both the LS - and jj -coupling schemes, even though the actual energy levels often lie between these two ideal scenarios due to the comparable energy scales of the Hund's coupling and SOC [11–13]. In the $5d^1$ systems, only one spin couples with the orbital so that both coupling schemes lead to a $J_{\text{eff}} = 3/2$ quartet with reduced dipolar moment sizes [14–25]. In the $5d^3$ systems such as Ba_2YOsO_6 and $\text{Sr}_2\text{ScOsO}_6$, an unusually large spin gap of approximately 18–19 meV has been observed in experiments [26–29]. This excitation gap cannot be explained in the LS -coupling scheme as it predicts an isotropic $S = 3/2$ ground-state manifold with gapless excitations. In the jj -coupling scheme, an excitation gap may emerge from the anisotropic exchange interactions that are enhanced by the SOC-induced $J_{\text{eff}} = 3/2$ ground-state manifold [26–30]. For the $5d^2$ compounds, both the LS - and jj -coupling schemes lead to a similar ground-state manifold of $J_{\text{eff}} = 2$ as illustrated in Fig. 2. In the LS -coupling scheme, antisymmetrized two-electron states within the t_{2g} manifold yield an effective total orbital angular momentum $L = 1$, which couples with a total spin $S = 1$ state favored by strong Hund's coupling. Moderate SOC then mixes the $L = 1$ and $S = 1$ states to produce low-energy multiplets of effective $J_{\text{eff}} = 2, 1, 0$. In contrast, in the jj -coupling scheme, each

*Contact author: dhirai@nuap.nagoya-u.ac.jp

†Contact author: sgao@ustc.edu.cn

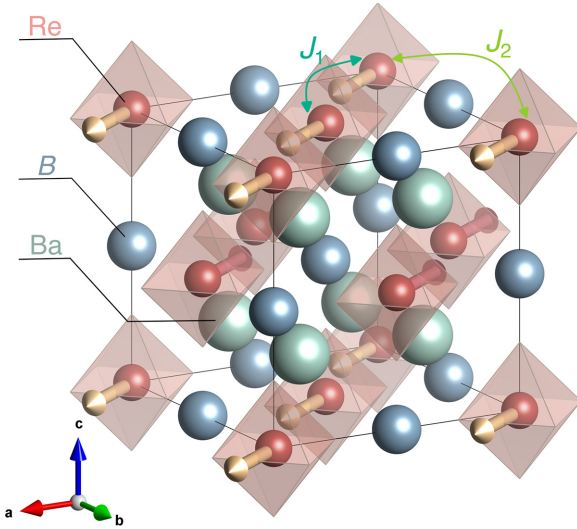


FIG. 1. Crystal structure of the double perovskites Ba_2BReO_6 ($B = \text{Y, Sc}$). The Ba, $B = \text{Y or Sc}$, and Re atoms are shown as green, blue, and red spheres, respectively. The oxygen atoms (not shown) form octahedra around the Re atoms. Exchange paths for the nearest-neighbor interaction J_1 and next-nearest-neighbor interaction J_2 are indicated by arrows. The type-I dipolar AFM order with $\mathbf{q} = (0, 0, 1)$ is indicated by yellow and pink arrows on each Re ion.

electron first experiences strong SOC so that the t_{2g} levels are split into the $j = 1/2$ and $j = 3/2$ states. The two-electron configuration favors $j_1 = j_2 = 3/2$, leading to allowed total states of $J_{\text{eff}} = 2, 0$, among which the $J_{\text{eff}} = 2$ manifold is energetically favored due to Hund's coupling. In the strong-SOC limit, the magnetic moment is reduced to approximately $1.225 \mu_B$ [31]. For both coupling schemes, the $J_{\text{eff}} = 2$ manifold can be further split by a residual crystal field into a non-Kramers E_g doublet and a T_{2g} triplet [32–34].

In contrast to conventional magnets with purely spin degrees of freedom, entangled spins and orbitals in the $5d$ -based DPs may allow for the possibility of multipolar interactions. The study of the multipolar orders, which are often described as “hidden orders” due to the difficulty in their direct experimental detection, has been mainly focused on f -electron systems [35,36]. Recent theoretical and experimental works suggest the importance of multipolar interactions in the $5d$ -electron systems. A notable example is the $5d^1$ compound

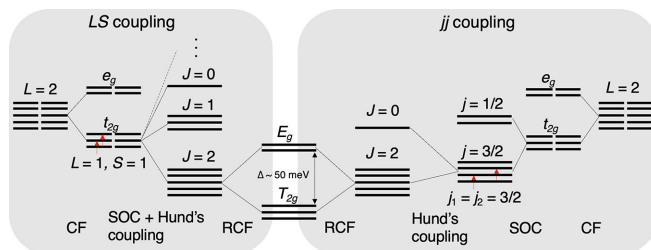


FIG. 2. Schematic illustration of the energy-level splitting of the $5d^2$ ion in the presence of an octahedral crystal field (CF), SOC, Hund's coupling, and a residual crystal field (RCF). Under both the LS - and jj -coupling schemes, the ground state of the $5d^2$ ion is a dipolar and quadrupolar active triplet T_{2g} manifold.

$\text{Ba}_2\text{MgReO}_6$ [16,18,20,21,23]. In this material, antiferroic $Q^{x^2-y^2}$ quadrupolar order and ferroic Q^{3z^2} quadrupolar order have been experimentally identified. The recent discovery of the dynamic Jahn-Teller effect, driven by the orbital degree of freedom, also induced further interest in this family of compounds [19,22,37–39]. For the $5d^1$ and $5d^2$ systems, a rich phase diagram has been predicted by some mean-field analysis, including the type-I antiferromagnetic (AFM) dipolar order, quadrupolar order, and a variety of octupolar orders [31,40,41]. Recently, ferro-octupolar orders have been proposed to emerge in the Os-based $5d^2$ DPs such as Ba_2MOsO_6 ($M = \text{Ca, Mg, Zn}$) [32]. This proposal is attributed to the absence of dipolar magnetic order and the lack of quadrupolar-related structural transitions. Many theoretical works on the $5d^2$ DPs have then been established under this framework [33,34,42–49]. However, AFM orders, albeit with reduced ordered moment sizes, are also experimentally observed in other $5d^2$ DPs [50–52], which calls for further experimental and theoretical studies. In particular, according to the mean-field analysis of the $5d^2$ DPs [31,41], quadrupolar orders may emerge at temperatures above the magnetic dipolar ordering transition, although conclusive evidence for their existence is still missing.

Our study focuses on two archetypal $5d^2$ Re-based double perovskites Ba_2YReO_6 and $\text{Ba}_2\text{ScReO}_6$. These two compounds share similar lattice geometry and electronic configurations. Previous experimental studies on Ba_2YReO_6 using muon spin rotation and neutron powder diffraction (NPD) yield conflicting conclusions regarding the existence of a long-range magnetic order [52–54], while studies on $\text{Ba}_2\text{ScReO}_6$ have been limited to its synthesis and basic structural characterizations [55].

Here, through magnetic susceptibility, heat capacity, neutron diffraction, and inelastic neutron scattering (INS) experiments on polycrystalline samples of Ba_2YReO_6 and $\text{Ba}_2\text{ScReO}_6$, we provide experimental evidence for the existence of a type-I dipolar AFM order in both compounds. Although our INS experiments on these two compounds reveal dominant phonon excitations as confirmed through the density functional theory (DFT) calculations, weak magnetic excitations can be identified, which are gapped in the dipolar ordered phase and softened in the correlated paramagnetic phase. Under the mean-field random phase approximation (MFRPA), a minimal model that incorporates both the dipolar and quadrupolar interactions is proposed to describe the temperature dependence of the spin dynamics, which supports the existence of a ferro-quadrupolar (FQ) order in these two compounds.

II. METHODS

Polycrystalline samples of Ba_2YReO_6 and $\text{Ba}_2\text{ScReO}_6$ were prepared by the conventional solid-state reaction [54,56]. BaO , Y_2O_3 (Sc_2O_3), and ReO_3 powders were mixed in a 4:1:2 ratio in an argon-filled glove box. The mixture was pelletized and placed in a platinum capsule in an evacuated quartz tube. The tube was heated at 1000°C for 50 h and then furnace cooled. The sintered pellet was crushed and re-pelletized in a glove box and then heated in an evacuated quartz tube at 1150°C for 50 h. The obtained pellet

had a dark blue color. The polycrystalline samples were characterized by x-ray diffraction (XRD) at ambient temperature in a diffractometer (SmartLab, Rigaku Corporation) with monochromatic Cu K_α radiation.

Magnetic susceptibility was measured using a magnetic property measurement system (MPMS3, Quantum Design). A polycrystalline pellet was attached to a quartz sample holder using varnish (GE7031, General Electric Company). Heat capacity measurements were conducted using a semiadiabatic thermal relaxation method on a physical property measurement system (PPMS, Quantum Design). Thermal contact between the sample and the sapphire sample stage was made using grease (Apiezon-N, M&I Materials Ltd).

Neutron diffraction experiments on powder samples of Ba_2YReO_6 and $\text{Ba}_2\text{ScReO}_6$ were performed on the POWGEN diffractometer [57] at the Spallation Neutron Source (SNS) of the Oak Ridge National Laboratory (ORNL) and the VERITAS (HB-1A) triple-axis spectrometer at the High Flux Isotope Reactor of the ORNL. For the experiments on POWGEN, about 8.5 g of powder of Ba_2YReO_6 and $\text{Ba}_2\text{ScReO}_6$ were filled into air-tight vanadium cans with a diameter of 8 mm in a helium-filled glove box. The POWGEN Automatic Changer was utilized to reach a base temperature of approximately 18 K. The neutron frame 2 with a center wavelength of 1.5 Å was used to collect the data, covering a wide Q region from 0.48 to 12.98 Å⁻¹. Data reduction was performed using the MANTID software [58]. For the experiments on the HB-1A instrument, the same powder samples were filled in vanadium sample cans with a diameter of 17 mm in a helium-filled glove box. An incoming neutron wavelength of $\lambda = 2.38$ Å was selected using a pyrolytic graphite (PG)(002) monochromator. A PG(002) analyzer was employed to ensure elastic scattering, leading to an energy resolution of 1 meV. A closed cycle refrigerator (CCR) cooling machine was utilized to reach the base temperature of 4 K.

INS experiments on powder samples of Ba_2YReO_6 and $\text{Ba}_2\text{ScReO}_6$ were performed on the SEQUOIA spectrometer [59] at the SNS. The same powder samples used for diffraction measurements were sealed in aluminum cans in a helium-filled glove box. A CCR cooling machine was utilized to reach a base temperature of 6 K. Measurements were taken with incident neutron energies of $E_i = 60$ meV in the high-flux chopper configuration with a Fermi chopper frequency of 120 Hz and $E_i = 225$ meV in the high-resolution chopper configuration with a Fermi chopper frequency of 600 Hz. For both measuring conditions, data were also collected using an empty can and subtracted as background. Data were histogrammed using the MANTID software [58] and further data reduction was performed using the MSLICE program in DAVE [60].

To understand the experimental results, we used the first-principles DFT technique as implemented on the Vienna *ab initio* simulation package with the projector augmented wave method [61–63]. Electronic correlations were considered by using the generalized gradient approximation with the Perdew-Burke-Ernzerhof potential [64]. Furthermore, the atomic positions were fully relaxed until the Hellmann-Feynman force on each atom was smaller than 0.001 eV/Å using the A-type magnetic state obtained in our neutron experiment, where the lattice constants were fixed as collected

in the diffraction data. In addition, the on-site interactions were considered by using the local spin-density approach plus U_{eff} ($U_{\text{eff}} = 2$ eV) with the Dudarev rotationally invariant formulation [65]. Then we calculated the force constants by using the density functional perturbation theory approach [66,67] and analyzed the phonon dispersion relations by the PHONOPY software [68,69]. Here the plane-wave cutoff energy was set as 600 eV and the k -point mesh was used as $4 \times 4 \times 4$ for the conventional cell for both Ba_2YReO_6 and $\text{Ba}_2\text{ScReO}_6$. The calculated data were convoluted with the instrumental energy resolution using the OCLIMAX program [70].

To analyze the INS spectra and the temperature evolution of the magnetic susceptibility, we employed the MFRPA [71–73]. This method allows for the calculation of spin excitations by treating the dipolar and quadrupolar interactions on an equal basis. The magnetic susceptibility calculations were performed with an energy step of 0.02 meV. For the calculation of the INS cross section, an energy step of 0.3 meV was used. The powder average of the calculated INS spectra was obtained by sampling 100 random points at each Q position in steps of 0.02 Å⁻¹. The resulting spectra were convoluted by the instrumental energy resolution function.

III. EXPERIMENTAL RESULTS

A. Crystal structure

Figure 3 presents the Rietveld refinement results of the XRD patterns collected at room temperature, along with the neutron diffraction patterns collected on POWGEN at $T = 300$ K. Tables I and II summarize the refined parameters of the neutron diffraction pattern for Ba_2YReO_6 and $\text{Ba}_2\text{ScReO}_6$, respectively. A tiny amount of $\text{Sc}_{2+x}\text{O}_{3+y}$ impurity phase with an estimated mass fraction of less than approximately 0.02 wt. % was identified in $\text{Ba}_2\text{ScReO}_6$, while no impurity phase was detectable in Ba_2YReO_6 . Throughout the entire temperature regime investigated, both Ba_2YReO_6 and $\text{Ba}_2\text{ScReO}_6$ stay in the cubic space group $Fm\bar{3}m$, as consistent with the previous report [54,55]. For the refinement of the neutron diffraction patterns, introducing off-stoichiometric occupancy does not improve the goodness of fit for Ba_2YReO_6 , while for $\text{Ba}_2\text{ScReO}_6$, the R factor decreases from 5.99% to 5.57% when the occupancy of the Sc and Re sites is fitted to 0.902(8) and 1.05(1). This defect in $\text{Ba}_2\text{ScReO}_6$ can be attributed to closer radii of the Sc^{3+} and Re^{5+} ions, which puts $\text{Ba}_2\text{ScReO}_6$ close to the stability boundary of the ordered double perovskites [10,74].

B. Magnetization

Figures 4(a) and 4(b) summarize the temperature dependence of the magnetic susceptibility $\chi(T)$ for Ba_2YReO_6 and $\text{Ba}_2\text{ScReO}_6$ measured in a field of 7 T. For Ba_2YReO_6 , a sudden drop in $\chi(T)$ is observed at $T_N = 31$ K, which suggests the existence of an AFM long-range-ordering transition at this temperature. At a slightly higher temperature of $T_q \sim 37$ K, an additional transition can be identified as the maximum of the $\chi(T)$ value. Similarly, in $\text{Ba}_2\text{ScReO}_6$, two transitions are observed at $T_N = 35$ K and $T_q \sim 50$ K. In the intermediate-temperature range between T_N and T_q , a plateau is observed,

TABLE I. Refined cell parameters and atomic positions of Ba₂YReO₆ using the diffraction data collected on POWGEN at $T = 300$ and 18 K.

Atom	300 K				18 K			
	x	y	z	$U_{\text{iso}} (\text{\AA}^2)$	x	y	z	$U_{\text{iso}} (\text{\AA}^2)$
Ba	0.25	0.25	0.25	0.0060(2)	0.25	0.25	0.25	0.0007(1)
Y	0.5	0.5	0.5	0.0053(3)	0.5	0.5	0.5	0.0006(2)
Re	0	0	0	0	0	0	0	0
O	0.23427(9)	0	0	0.0087(2)	0.23427(6)	0	0	0.0036(1)
a	8.37091(2)				8.36033(2)			
R_p	7.67%				8.52%			
R_{wp}	10.50%				11.72%			

which is more pronounced in Ba₂ScReO₆. To better elucidate the magnetic transition and compare with the heat capacity data in the next section, we plot the $d(\chi T)/dT$, i.e., the Fisher relation [75], in the insets of Figs. 4(a) and 4(b). It reveals a clear maximum for Ba₂YReO₆ at $T_N = 31$ K, while for Ba₂ScReO₆, a broader peak with a maximum at $T_N = 32.5$ K is observed. According to mean-field calculations, the two successive transitions at T_N and T_q may correspond to the magnetic dipolar and quadrupolar long-range-order transitions, respectively [31,41]. Figures 4(c) and 4(d) present the inverse magnetic susceptibility data for Ba₂YReO₆ and Ba₂ScReO₆. The red solid line is the Curie-Weiss fit of the magnetic susceptibility in the high-temperature regime of 150–300 K. At temperatures above 150 K, both DPs display well-defined Curie-Weiss behavior, yielding an effective magnetic moment $\mu_{\text{eff}} = 2.16 \mu_B$ and Weiss temperature $\Theta_W = -584(1)$ K for Ba₂YReO₆, and $\mu_{\text{eff}} = 1.98 \mu_B$ and $\Theta_W = -570(1)$ K for Ba₂ScReO₆. At $T \sim 60$ K for Ba₂YReO₆ and $T \sim 100$ K for Ba₂ScReO₆, a deviation from the Curie-Weiss behavior is observed, which suggests the development of short-range fluctuations. A similar phenomenon has also been observed in the previous report for Ba₂YReO₆ with fitted $\mu_{\text{eff}} = 1.93 \mu_B$ and $\Theta_W = -616(7)$ K [54]. The reduced effective moment size, which is lower than the spin-only value of $2.83 \mu_B$, indicates a significant compensation from the orbital moment. It is noteworthy that the Weiss temperatures for Ba₂YReO₆ and Ba₂ScReO₆ are approximately four times higher than that of Ba₂CaOsO₆, a closely related $5d^2$ compound that does not exhibit magnetic dipolar order at low temperatures [32].

TABLE II. Refined cell parameters and atomic positions of Ba₂ScReO₆ using the diffraction data collected on POWGEN at $T = 300$ and 18 K.

Atom	300 K				18 K			
	x	y	z	$U_{\text{iso}} (\text{\AA}^2)$	x	y	z	$U_{\text{iso}} (\text{\AA}^2)$
Ba	0.25	0.25	0.25	0.0053(2)	0.25	0.25	0.25	0.0033(1)
Sc	0.5	0.5	0.5	0.0039(4)	0.5	0.5	0.5	0.0061(2)
Re	0	0	0	0.0047(5)	0	0	0	0
O	0.2429(2)	0	0	0.0083(1)	0.2425(1)	0	0	0.0069(1)
Occupancy (Sc)	0.902(8)				0.902			
Occupancy (Re)	1.05(1)				1.05			
a	8.16177(2)				8.15103(2)			
R_p	5.72%				7.04%			
R_{wp}	7.97%				8.04%			

C. Heat capacity

Figure 5 presents the temperature evolution of the normalized heat capacity $C(T)/T$ for Ba₂YReO₆ and Ba₂ScReO₆. The transition temperature for both compounds is consistent with the magnetization measurements. For Ba₂YReO₆, $C(T)/T$ exhibits a sharp λ -shaped peak at $T_N = 31$ K, which was not observed in the previous report [54,56]. This difference may arise from the improved quality of our synthesized sample: In our experiments, we observe that a higher sintering temperature improves the crystallization and leads to a more pronounced transition in $C(T)$. An additional transition at approximately 35 K is observed for Ba₂YReO₆ in Fig. 5(c), which is close to the transition at $T_q = 37$ K in $\chi(T)$. For Ba₂ScReO₆, a relatively weak peak is observed at 33.5 K, which is close to the AFM transition at $T_N = 35$ K in $\chi(T)$ shown in Fig. 4(b). Further attempts to improve the crystallization of the Ba₂ScReO₆ sample through increased sintering temperature were not successful. As discussed in Sec. III A, Ba₂ScReO₆ lies near the stability boundary of the rocksalt ordered phase, making it challenging to obtain high-quality samples.

D. Magnetic order

Neutron diffraction data for powder samples of Ba₂YReO₆ and Ba₂ScReO₆ were collected on POWGEN at $T = 18, 32,$ and 300 K. As shown in Figs. 6(a) and 6(b), at $T = 18$ K, magnetic Bragg peaks belonging to the propagation vector $\mathbf{q} = (0, 0, 1)$ are observed. For both samples, the magnetic structures are refined to be a type-I dipolar AFM order as

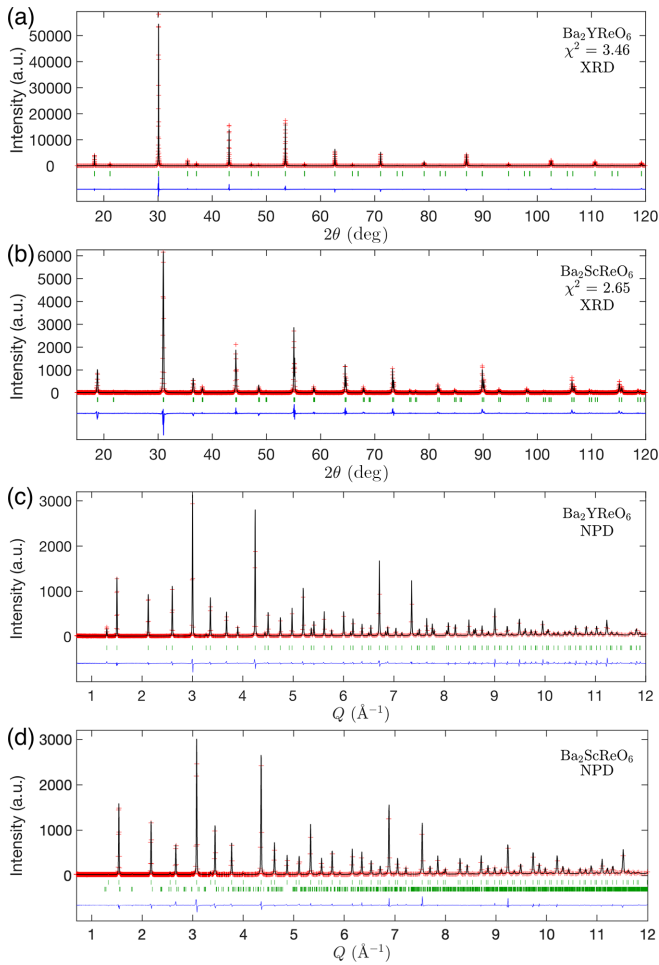


FIG. 3. Refinement results of the x-ray diffraction data for (a) Ba_2YReO_6 and (b) $\text{Ba}_2\text{ScReO}_6$ at $T = 300$ K and refinement results of the neutron diffraction data for (c) Ba_2YReO_6 and (d) $\text{Ba}_2\text{ScReO}_6$ at room temperature. Red pluses represent the observed data points, the black solid line corresponds to the calculated pattern, and the blue solid line shows the difference between the observed and calculated patterns. The green ticks indicate the positions of nuclear Bragg reflections. For $\text{Ba}_2\text{ScReO}_6$, the lower row of green ticks in (d) indicates the presence of tiny $\text{Sc}_{2+x}\text{O}_{3+y}$ impurity, for which the diffraction intensity was calculated by the Le Bail method.

described in Fig. 1. The magnetic form factor of the Re^{5+} ions as reported in Ref. [76] is employed for our refinements. For Ba_2YReO_6 and $\text{Ba}_2\text{ScReO}_6$, the ordered dipolar moment sizes are refined to be $0.41(4) \mu_B$ and $0.3(2) \mu_B$, respectively. These refined moment sizes are consistent with the refined value in the previous polarized NPD experiment for Ba_2YReO_6 [52] and are also close to the predicted values in the DFT calculations [77,78]. The reduced ordered moment size in Ba_2YReO_6 and $\text{Ba}_2\text{ScReO}_6$ may result from a competition between the dipolar and quadrupolar orders [52,79], which is also discussed in the following section on MFRPA analysis. Neutron diffraction data were also collected on HB-1A at $T = 4, 60,$ and 80 K as shown in Figs. 6(c) and 6(d), which reveal the same magnetic Bragg peaks from the POWGEN experiments. As further evidence of the existence of a dipolar long-range order at low temperatures, Figs. 6(e) and 6(f) present the elastic signals obtained by integrating the SE-

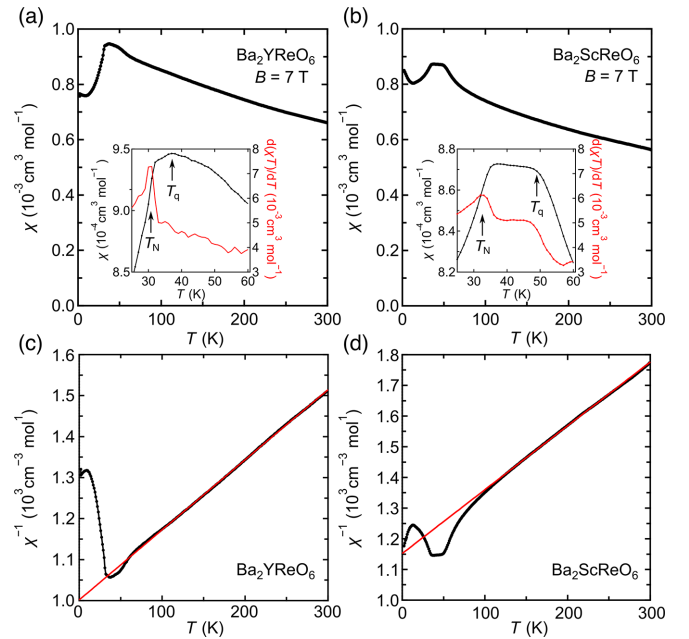


FIG. 4. Temperature evolution of the magnetic susceptibility $\chi(T)$ for (a) Ba_2YReO_6 and (b) $\text{Ba}_2\text{ScReO}_6$ measured in a 7 T field. The inset is an enlarged view of the low-temperature regime with the red solid line corresponding to the Fisher heat capacity $d(\chi T)/dT$. The inverse magnetic susceptibility $\chi^{-1}(T)$ is plotted for (c) Ba_2YReO_6 and (d) $\text{Ba}_2\text{ScReO}_6$. The red solid line is the Curie-Weiss fit for the magnetic susceptibility in the high-temperature regime of 150–300 K.

QUOIA data in the energy transfer range of $[-1.5, 1.5]$ meV. At $T = 6$ K, magnetic peaks of $(0, 0, 1)$ and $(1, 1, 0)$ are observed for both samples. Magnetic structural refinements were performed for the data collected at $T = 6$ K with the data collected at $T = 180$ K being subtracted as the background. The refinement results are summarized in Figs. 6(g) and 6(h). The refined ordered moment sizes are $0.47(1) \mu_B$ and $0.52(2) \mu_B$

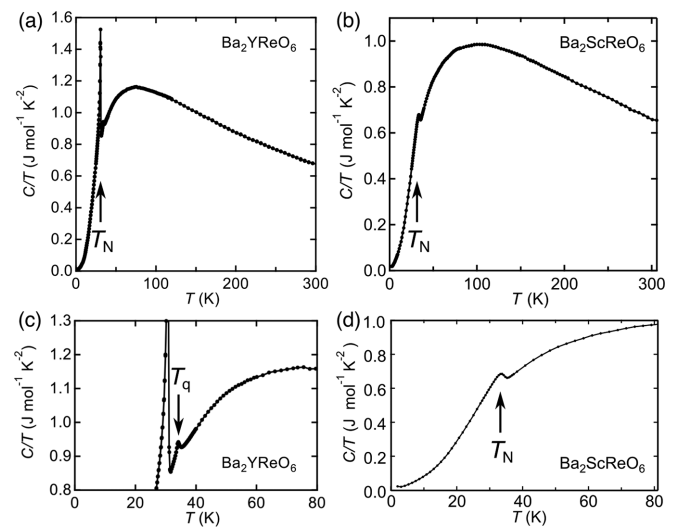


FIG. 5. Temperature evolution of the normalized heat capacity $C(T)/T$ for (a) Ba_2YReO_6 and (b) $\text{Ba}_2\text{ScReO}_6$. A zoomed-in view of the data in the low-temperature regime is shown for (c) Ba_2YReO_6 and (d) $\text{Ba}_2\text{ScReO}_6$.

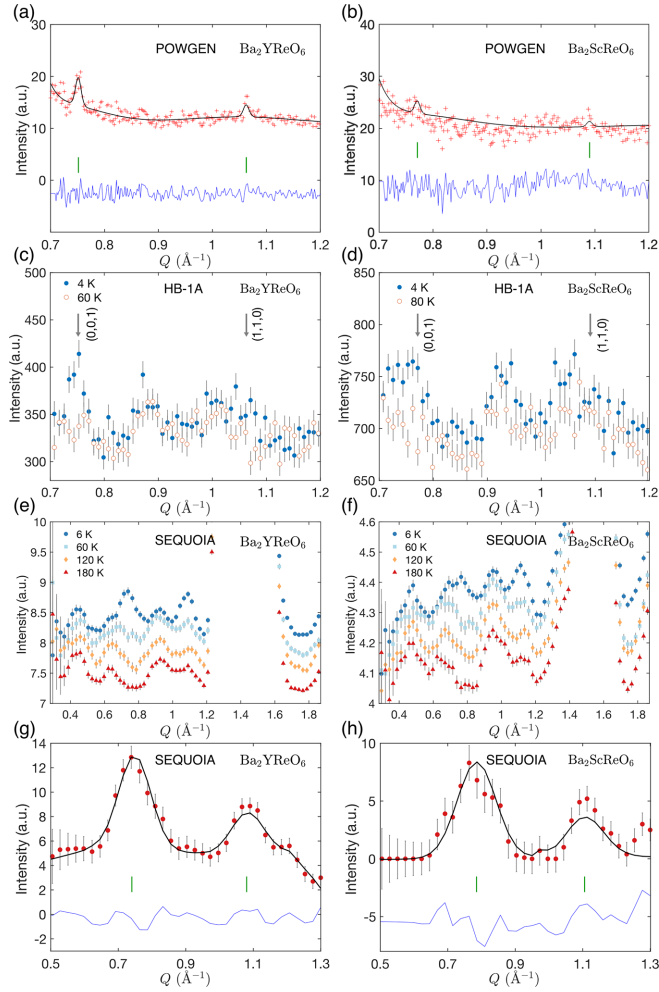


FIG. 6. Refinement results of the NPD data collected on POWGEN at $T = 18$ K for (a) Ba_2YReO_6 and (b) $\text{Ba}_2\text{ScReO}_6$. Symbols in the figure are the same in Fig. 3. Green ticks highlight the magnetic Bragg peaks at $(0, 0, 1)$ and $(1, 1, 0)$. The NPD data were collected on HB-1A at $T = 4, 60,$ and 80 K for (c) Ba_2YReO_6 and (d) $\text{Ba}_2\text{ScReO}_6$, respectively. (e) and (f) Temperature dependence of the elastic signals obtained by integrating the $E_i = 60$ meV SEQUOIA data in an energy transfer range of $[-1.5, 1.5]$ meV at $T = 6, 60, 120,$ and 180 K. For Ba_2YReO_6 , data are offset by $0, 0.1, 0.2,$ and 0.3 at $6, 60, 120,$ and 180 K, respectively. For $\text{Ba}_2\text{ScReO}_6$, data are offset by $0, 0.05, 0.1,$ and 0.2 at $6, 60, 120,$ and 180 K, respectively. (g) and (h) Rietveld refinements were performed on the difference data obtained by subtracting the 180 K data from the 6 K data on SEQUOIA for both DPs. The red points represent the observed data, the black solid line corresponds to the calculated pattern, and the blue solid line below shows the difference between the observed and calculated patterns. The vertical green ticks indicate the positions of magnetic peaks.

for Ba_2YReO_6 and $\text{Ba}_2\text{ScReO}_6$, respectively. The difference in the ordered moment size compared to the values refined from the POWGEN data is likely due to their different measuring temperatures. Similar magnetic diffraction patterns have also been observed in other $5d^2$ DPs [50,51]. Meanwhile, at elevated temperatures of 32 and 300 K, as shown in Fig. 7, the magnetic Bragg peaks disappear, which indicates the transition at 35 K in the specific-heat data is not of a dipolar origin.

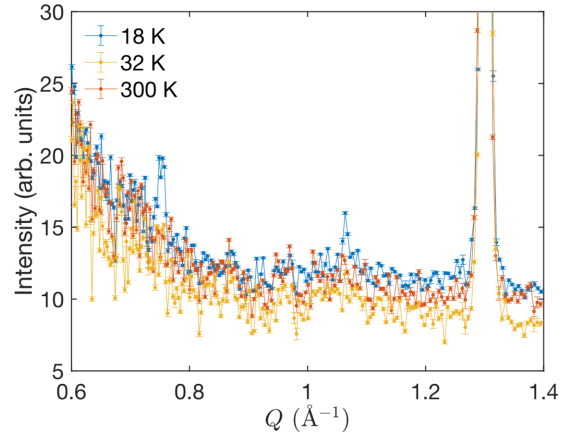


FIG. 7. Temperature dependence of the neutron diffraction data for Ba_2YReO_6 collected on POWGEN at $T = 18, 32,$ and 300 K. Error bars are shown but are smaller than symbol sizes for most data in the figure.

E. Phonon and magnon excitations

Figures 8(a)–8(d) present the INS data for Ba_2YReO_6 and $\text{Ba}_2\text{ScReO}_6$ collected on SEQUOIA at $T = 6$ K with incident energies $E_i = 60$ and 225 meV. As can be inferred from the wave-vector dependence, the phonon density of states dominates the spectra, overshadowing other possible contributions such as magnetic excitations. Figures 8(e)–8(h) present the theoretical phonon excitations calculated by the DFT, based on the lattice parameters as refined from the neutron diffraction data. The spectra have been convoluted by the instrumental energy resolution function. The calculated spectra reproduce the main features of the experimental results. However, in the low-wave-vector transfer regime ($Q < 2 \text{ \AA}^{-1}$), between 10 and 20 meV, weak scattering is observed in experiments, which is not captured by the DFT calculations. These features may originate from magnetic excitations. Figures 9(a)–9(d) present the zoomed-in view of the INS spectra for Ba_2YReO_6 and $\text{Ba}_2\text{ScReO}_6$ collected at temperatures of $T = 6$ and 60 K. Compared to the 6 K data, softened magnetic excitations at $T = 60$ K can be observed at $Q \sim 0.75 \text{ \AA}^{-1}$, the same position for the magnetic Bragg peak at $(0, 0, 1)$, for energy transfers below 10 meV, a behavior that has been observed in other $5d$ -based DPs [27–29,32,50]. Therefore, we conclude that at the base temperature of $T = 6$ K, the magnetic scattering in the dipolar ordered phase is either out of the detectable area or overshadowed by the phonon excitations. Figures 9(e) and 9(f) illustrate the temperature evolution of the scattering intensity integrated in the range of $[5.5, 8.5]$ meV as a function of the wave-vector transfer. At temperatures of $60, 120,$ and 180 K, the intensity at $Q \sim 0.75 \text{ \AA}^{-1}$ becomes significantly enhanced, which strongly evidences the existence of softened magnetic excitations at temperatures above the dipolar long-range-ordering transition.

IV. MFRPA ANALYSIS

Using the MFRPA method, we propose a minimal model to describe the dipolar and quadrupolar correlations in Ba_2YReO_6 and $\text{Ba}_2\text{ScReO}_6$. In our model, we start from

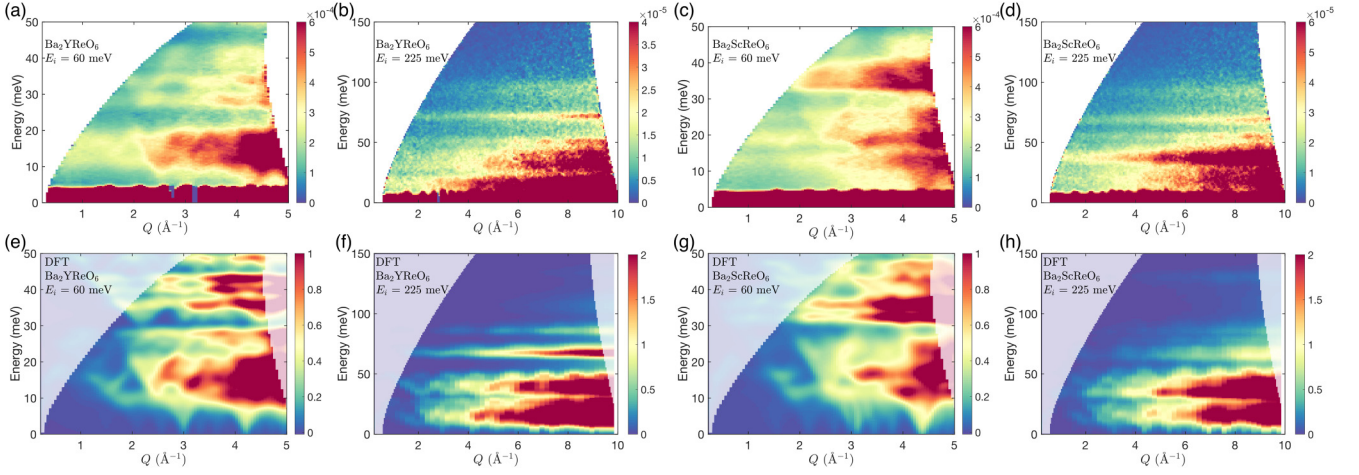


FIG. 8. (a)–(d) INS data collected on SEQUOIA at $T = 6$ K for Ba_2YReO_6 and $\text{Ba}_2\text{ScReO}_6$ with incident energies $E_i = 60$ meV and 225 meV. (e)–(h) Calculated phonon spectra convolved by the corresponding instrumental energy resolution functions.

the single-ion electronic configuration of the Re^{5+} ions. The couplings among the Re^{5+} ions include dominant AFM J_1 over the nearest neighbors, relatively weak ferromagnetic J_2 over the next-nearest neighbors, and quadrupolar interactions K over the nearest neighbors. The exchange paths for the nearest- and next-nearest-neighbor couplings are indicated in Fig. 1.

The Hamiltonian of our minimal model is expressed as

$$\mathcal{H} = \sum_i \mathcal{H}_{\text{SI}}^i + \mathcal{H}_I, \quad (1)$$

where $\mathcal{H}_{\text{SI}}^i$ represents the single-ion Hamiltonian at site i and \mathcal{H}_I describes the inter-ion interactions.

A. Single-ion Hamiltonian

As discussed in the Introduction, the effective ground state of a Re^{5+} ion in a strong octahedral crystal field is a SOC-induced $J_{\text{eff}} = 2$ manifold. Within this manifold, the single-ion Hamiltonian on site i is expressed as

$$\mathcal{H}_{\text{SI}}^i = \mathcal{H}_{\text{RCF}} + \mathcal{H}_W. \quad (2)$$

In this expression, \mathcal{H}_{RCF} represents the residual crystal field that splits the $J_{\text{eff}} = 2$ manifold into the T_{2g} triplet and the E_g doublet as shown in Fig. 2. As discussed in Refs. [32–34], this term arises from the higher-order perturbations and the nonspherical Coulomb interactions, which can be described as

$$\mathcal{H}_{\text{RCF}} = -\frac{\Delta}{120} (\mathcal{O}_4^0 + 5\mathcal{O}_4^4), \quad (3)$$

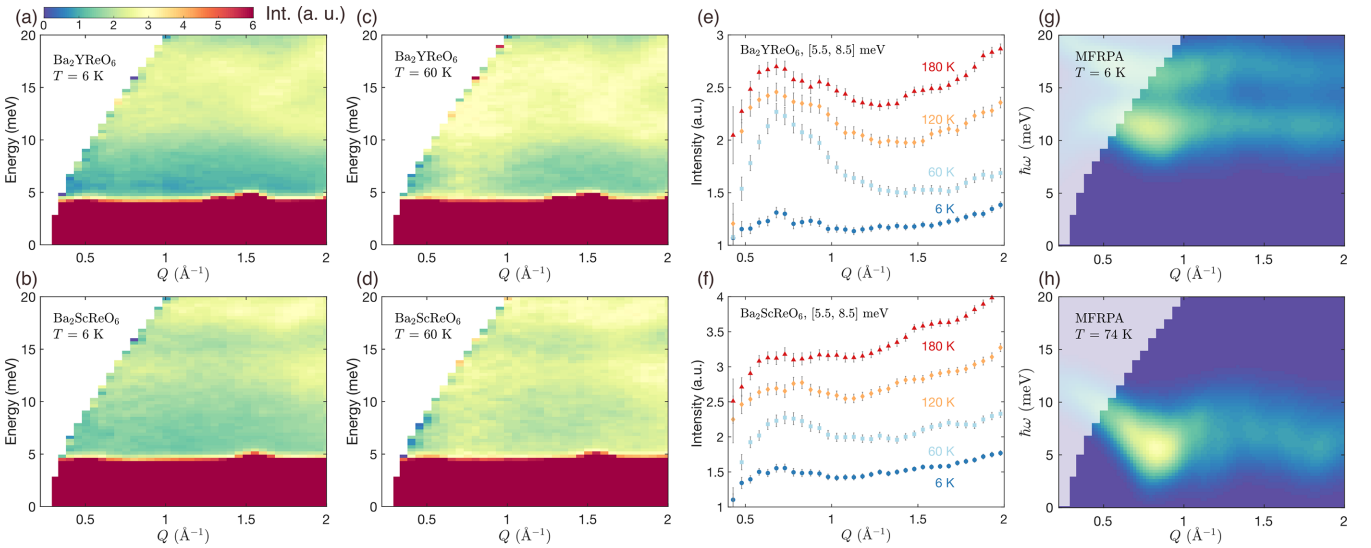


FIG. 9. (a)–(d) INS spectra collected at $T = 6$ and 60 K for Ba_2YReO_6 and $\text{Ba}_2\text{ScReO}_6$ with incident energy $E_i = 60$ meV. (e) and (f) Temperature evolution of the integrated intensity in the energy range of [5.5, 8.5] meV as a function of the wave-vector transfer. (g) and (h) Simulated INS spectra using the MFRPA method for the minimal model at $T = 6$ and 74 K. At low temperatures, the excitation is gapped by approximately 10 meV. At $T = 74$ K, in the FQ phase, magnetic excitations are observed at $Q \sim 0.75 \text{ \AA}^{-1}$, which is consistent with the experimental observations at elevated temperatures.

where the Steven operators are defined as

$$\begin{aligned} \mathcal{O}_4^0 &= 35J_z^4 - [30J(J+1) - 25]J_z^2 + 3J^2(J+1)^2 \\ &\quad - 6J(J+1), \\ \mathcal{O}_4^4 &= \frac{1}{2}(J_+^4 + J_-^4). \end{aligned} \quad (4)$$

Here we choose negative Δ so that the energy of the triplet is lower than that of the doublet in the reversed level scheme as suggested for Ba_2YReO_6 [34]. For our semiquantitative analysis, Δ is set to -50 meV based on the experimental Curie-Weiss temperature. This choice is justified as the high-Curie-Weiss-temperature behavior is strongly impacted by the single-ion physics [34]. Adjustment of the exact value of Δ in a broad range of $[-100, -35]$ meV does not impact the conclusion of our analysis. We have also considered the case of $\Delta > 0$, but no satisfactory results were obtained. The second term in \mathcal{H}_{SI} represents a weak Weiss field \mathcal{H}_W , which accounts for the symmetry-broken term of the quadrupolar order. It is defined as

$$\mathcal{H}_W = \lambda Q^{3z^2} = \lambda[3J_z^2 - J(J+1)]/\sqrt{3}, \quad (5)$$

where λ is a small constant that describes the strength of the Weiss field.

B. Inter-ion interactions

The exchange interactions among the Re^{5+} ions are described by the inter-ion Hamiltonian \mathcal{H}_I ,

$$\begin{aligned} \mathcal{H}_I &= \sum_{ij} \sum_{\alpha,\beta} \mathcal{J}_{\alpha\beta}(\Delta\mathbf{R}_{i,j}) \mathcal{I}_\alpha^i \mathcal{I}_\beta^j \\ &= \sum_{\langle i,j \rangle} (J_1 \mathbf{J}_i \cdot \mathbf{J}_j + K Q^{3z^2,i} \cdot Q^{3z^2,j}) + J_2 \sum_{\langle\langle i,j \rangle\rangle} \mathbf{J}_i \cdot \mathbf{J}_j, \end{aligned} \quad (6)$$

where $\langle i,j \rangle$ and $\langle\langle i,j \rangle\rangle$ denote the nearest-neighbor (NN) and next-nearest-neighbor (NNN) interactions, respectively, \mathcal{I}_α^s are the multipolar tensor operators $\mathcal{I} = (J^x, J^y, J^z, Q^{3z^2}, Q^{x^2-y^2})$ as defined in Refs. [35,40] within the $J_{\text{eff}} = 2$ manifold, and $\mathcal{J}_{\alpha\beta}(\Delta\mathbf{R}_{i,j})$ is the interaction matrix element between the α and β operators, with $\Delta\mathbf{R}_{i,j} = \mathbf{R}_i - \mathbf{R}_j$ the vector connecting sites i and j . In the matrix form, the couplings over the nearest and next-nearest neighbors can be expressed as

$$\mathcal{J}_{\text{NN}} = \begin{pmatrix} J_1 & 0 & 0 & 0 & 0 \\ 0 & J_1 & 0 & 0 & 0 \\ 0 & 0 & J_1 & 0 & 0 \\ 0 & 0 & 0 & K & 0 \\ 0 & 0 & 0 & 0 & 0 \end{pmatrix}, \quad (7)$$

$$\mathcal{J}_{\text{NNN}} = \begin{pmatrix} J_2 & 0 & 0 & 0 & 0 \\ 0 & J_2 & 0 & 0 & 0 \\ 0 & 0 & J_2 & 0 & 0 \\ 0 & 0 & 0 & 0 & 0 \\ 0 & 0 & 0 & 0 & 0 \end{pmatrix}. \quad (8)$$

C. Mean-field analysis of the ground state

The interactions on a single ion can be approximated using the mean-field method. Following our experimental observation of a type-I dipolar AFM ground state, the mean-field

Hamiltonian $\mathcal{H}_{\text{MF}}^s$ can be defined on two sublattices as

$$\mathcal{H}_{\text{MF}}^s = - \sum_{\alpha=1}^m H_\alpha^s \mathcal{I}_\alpha^s, \quad (9)$$

$$H_\alpha^s = \sum_{s',\alpha} \mathcal{J}_{\alpha\beta}(\Delta\mathbf{R}_{s,s'}) \langle \mathcal{I}_\beta^{s'} \rangle, \quad (10)$$

where s represents different sublattices and the summation includes all NN and NNN interactions. This mean-field Hamiltonian can be solved self-consistently to obtain the ordering behavior of both the dipolar and quadrupolar moments.

D. Generalized susceptibility

From the self-consistently determined mean-field ground state, one can calculate the single-ion susceptibility for each sublattice s . According to the linear response theory,

$$\chi_{\alpha\beta}^{0,s}(\omega) = \sum_{ij} \frac{\langle \Psi_i | \mathcal{I}_\alpha - \langle \mathcal{I}_\alpha | \Psi_j \rangle \langle \Psi_j | \mathcal{I}_\beta - \langle \mathcal{I}_\beta | \Psi_i \rangle | \Psi_i \rangle}{\epsilon_j - \epsilon_i - \hbar\omega} (p_i - p_j), \quad (11)$$

where $|\Psi_i\rangle$ and ϵ_i are the eigenstates and eigenvalues of the single-ion Hamiltonian at site s , respectively, and $p_i = \frac{\exp(-\epsilon_i/k_B T)}{\sum_j \exp(-\epsilon_j/k_B T)}$ is the thermal population factor, with k_B denoting the Boltzmann constant.

The generalized susceptibility can be calculated using the RPA method [71–73]. This method is widely used in the analysis of spin dynamics and has proven to be particularly successful in the study of multipolar interactions in the rare-earth systems [71,72,80–82]. Recently, it has also been applied to the study of the $5d$ heavy transition-metal compounds [30,44]. Under the RPA, the total generalized susceptibility is determined as

$$\chi_{\alpha\beta}(\mathbf{Q}, \omega) = \sum_{s,s'} \chi_{\alpha\beta}^{0,s}(\omega) [\delta^{ss'} - \chi_{\alpha\beta}^{0,s}(\omega) \mathcal{J}_{\alpha\beta}^{ss'}(\mathbf{Q})]^{-1}, \quad (12)$$

where $\delta^{ss'}$ is the Kronecker tensor and $\mathcal{J}_{\alpha\beta}^{ss'}(\mathbf{Q})$ is the Fourier transform of the exchange interaction matrix element $\mathcal{J}_{\alpha\beta}(\mathbf{R}_s - \mathbf{R}_{s'})$.

The real $[\chi'(\mathbf{Q}, \omega)]$ and imaginary $[\chi''(\mathbf{Q}, \omega)]$ parts of the generalized susceptibility can be calculated separately following Eq. (12). They are related by the Kramers-Kronig transformation [73] as

$$\chi'(\mathbf{Q}, 0) = \frac{1}{\pi} \int_{-\infty}^{\infty} \frac{\chi''(\mathbf{Q}, \omega)}{\omega} d\omega. \quad (13)$$

The magnetic susceptibility as probed in our experiments can be calculated from the real part [73] as

$$\chi_M = \frac{V}{\mu_0} \chi'(0, 0). \quad (14)$$

The INS cross section can be calculated from the imaginary part according to the fluctuation-dissipation theorem,

$$\begin{aligned} S(\mathbf{Q}, \omega) &\propto \sum_{\alpha,\beta=1,2,3} (\delta_{\alpha\beta} - \hat{Q}_\alpha \hat{Q}_\beta) \\ &\quad \times \left(\sum_{\mu,\mu'} F_{\alpha\mu}(\mathbf{Q}) F_{\beta\mu'}(\mathbf{Q}) \chi''_{\mu\mu'}(\mathbf{Q}, \omega) \right), \end{aligned} \quad (15)$$

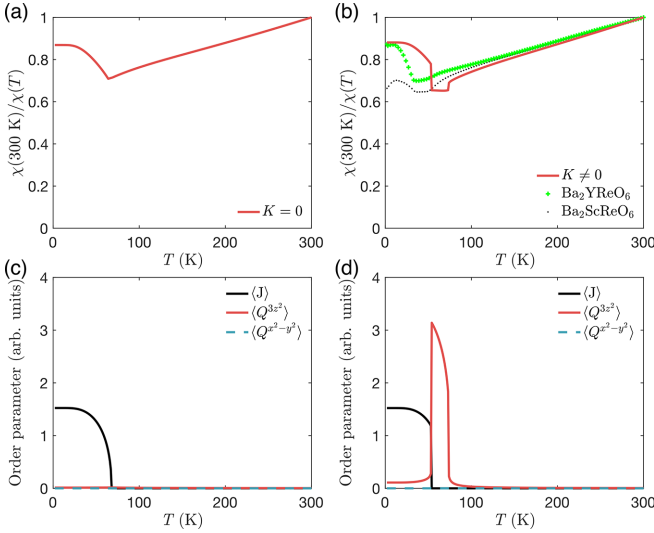


FIG. 10. (a) and (b) Temperature dependence of the normalized inverse magnetic susceptibility $\chi(300\text{ K})/\chi(T)$, where $\chi(300\text{ K})$ is the susceptibility at $T = 300\text{ K}$. The red solid line represents the calculation. Green pluses and black dots reproduce the experimental results for Ba_2YReO_6 and $\text{Ba}_2\text{ScReO}_6$ as shown in Fig. 4. In (a), a model with $K = 0$ shows only dipolar AFM transition. In (b), the minimal model including quadrupolar interaction K reproduces the experimentally observed plateau. Also shown is the temperature dependence of the order parameters for (c) the model with $K = 0$ and (d) the minimal model.

where μ and μ' sum over the components of the multipolar tensor operators and $F(\mathbf{Q})$ is the form factor of the multipolar tensor operator. In our case, this form factor can be simplified to a dipolar form factor $F^2(Q)$ since the quadrupolar interaction does not contribute to the form factor [44],

$$S(\mathbf{Q}, \omega) \propto \sum_{\alpha, \beta=1,2,3} (\delta_{\alpha\beta} - \hat{Q}_\alpha \hat{Q}_\beta) F^2(Q) \left(\sum_{\alpha\beta} \chi''_{\alpha\beta}(\mathbf{Q}, \omega) \right). \quad (16)$$

E. Applications to Ba_2YReO_6 and $\text{Ba}_2\text{ScReO}_6$

Figure 10 presents the calculated temperature dependence of the inverse magnetic susceptibility $\chi(300\text{ K})/\chi(T)$ and the order parameters using the MFRPA method. The order parameters are defined as

$$\langle J \rangle = \frac{1}{2} |\langle \mathbf{J}^1 \rangle - \langle \mathbf{J}^2 \rangle|, \quad (17)$$

$$\langle Q^{3z^2} \rangle = \frac{1}{2} |\langle Q^{3z^2,1} \rangle + \langle Q^{3z^2,2} \rangle|, \quad (18)$$

$$\langle Q^{x^2-y^2} \rangle = \frac{1}{2} |\langle Q^{x^2-y^2,1} \rangle + \langle Q^{x^2-y^2,2} \rangle|, \quad (19)$$

where the last index in the superscript represents the sublattices 1 and 2. The parameters for the calculations, including the coupling strengths, are listed in Table III. The magnetic susceptibility and order parameters for the minimal model in Fig. 10(b) exhibit two transitions, consistent with our experimental observations for Ba_2YReO_6 and $\text{Ba}_2\text{ScReO}_6$. In contrast, models with quadrupolar interaction $K = 0$ in Fig. 10(a) show only one transition that corresponds to the

TABLE III. Main parameters for the minimal model. All parameters are shown in units of meV.

Parameter	Value
Δ	-50
J_1	1.15
$J_2 = -0.2J_1$	-0.23
$K = -0.07J_1$	-0.0805
λ	-0.015

dipolar order. Compared to the experiments, the transition temperatures are overestimated, possibly due to the limitation of the mean-field approximations. At 100 K, the quadrupolar moment Q^{3z^2} starts to develop a ferroic order as shown in Fig. 10(d), causing the magnetic susceptibility to deviate from the Curie-Weiss behavior. Between 53 and 75 K, $\chi(300\text{ K})/\chi(T)$ forms a plateau, similar to the experimental results in Fig. 4. This intermediate phase is associated with the FQ order as evidenced by the finite quadrupolar moment Q^{3z^2} in Fig. 10(d), which is triggered by the quadrupolar interactions. This phase does not appear in the $K = 0$ case as illustrated in Fig. 10(c). At 53 K, the system transitions into a type-I dipolar AFM state as indicated by the evolution of the order parameter $\langle J \rangle$. The quadrupolar moment remains ferroic ordered even in the AFM phase at low temperatures in our minimal model, although its ordered moment size becomes greatly reduced due to the competition with the dipolar order.

The calculated INS spectra for the same minimal model, with the parameters from Table III, are shown in Figs. 9(g) and 9(h). At $T = 6\text{ K}$, the magnetic excitations are gapped, which is consistent with the experiments. In the FQ state at $T = 74\text{ K}$, the excitation band shifts towards the elastic line, leading to low-energy excitations that are very similar to the experimental INS spectra as shown in Figs. 9(c) and 9(d). At higher temperatures, the experimental INS spectra are determined by short-range correlations that are not captured in our mean-field analysis.

It is noteworthy that the actual interactions in Ba_2YReO_6 and $\text{Ba}_2\text{ScReO}_6$ can be more complicated than those considered in our minimal model. For instance, in systems with strong SOC, anisotropic interactions between the multipolar moments may play a significant role [30,44,82]. Refinement of a complete set of the parameters described in our Hamiltonian is beyond the quality of the data. The phonon contribution to the scattering and the powder averaged spectrum only allow for a qualitative comparison of these terms. However, our minimal model is able to reproduce the main features of the experimental results and provides a good starting point for further studies on the multipolar correlations in the $5d^2$ double perovskites.

V. CONCLUSION

We have performed magnetic susceptibility, heat capacity, and neutron scattering experiments on the $5d^2$ rhenium-based DP compounds Ba_2YReO_6 and $\text{Ba}_2\text{ScReO}_6$ to study their dipolar and quadrupolar correlations. Both compounds exhibit a type-I dipolar AFM ground state with a propagation vector $\mathbf{q} = (0, 0, 1)$, where the ordered moment size is

significantly reduced due to SOC and quadrupolar correlations. Our INS experiments reveal dominant phonon excitations, which are well described by the DFT calculations. Weak magnetic excitations with an excitation gap are observed at low temperatures, which become softened at elevated temperatures. Using the MFRPA method, a minimal model that considers both the dipolar and quadrupolar interactions is proposed to explain the susceptibility data and INS spectra, which evidence the existence of a FQ order in both the paramagnetic phase and the AFM ordered ground state.

ACKNOWLEDGMENTS

This work was supported by the U.S. Department of Energy, Office of Science, Basic Energy Sciences, Materials Sciences and Engineering Division (Neutron scattering data collection and initial analysis). This research used resources at the Spallation Neutron Source and the High Flux Isotope Re-

actor, both of which are DOE Office of Science User Facilities operated by the Oak Ridge National Laboratory. The beam time was allocated to POWGEN on Proposal No. IPTS-27345, to SEQUOIA on Proposal No. IPTS-26621, and to HB-1A on Proposal No. IPTS-26600. Work at USTC was funded by the National Key Research and Development Program of China under Grant No. 2024YFA1613100 and the National Natural Science Foundation of China under Grant No. 12374152. This work was also supported by the Japan Society for the Promotion of Science KAKENHI under Grants No. JP20H01858, No. JP23H04860, and No. JP24H01187 and the JSPS Bilateral Open Partnership Joint Research Project No. JPJSBP120239915.

DATA AVAILABILITY

The data that support the findings of this article are openly available [83].

-
- [1] W. Witczak-Krempa, G. Chen, Y. B. Kim, and L. Balents, Correlated quantum phenomena in the strong spin-orbit regime, *Annu. Rev. Condens. Matter Phys.* **5**, 57 (2014).
- [2] G. V. Chen and C. Wu, Multiflavor Mott insulators in quantum materials and ultracold atoms, *npj Quantum Mater.* **9**, 1 (2024).
- [3] T. Takayama, J. Chaloupka, A. Smerald, G. Khaliullin, and H. Takagi, Spin-orbit-entangled electronic phases in $4d$ and $5d$ transition-metal compounds, *J. Phys. Soc. Jpn.* **90**, 062001 (2021).
- [4] B. J. Kim, H. Jin, S. J. Moon, J.-Y. Kim, B.-G. Park, C. S. Leem, J. Yu, T. W. Noh, C. Kim, S.-J. Oh, J.-H. Park, V. Durairaj, G. Cao, and E. Rotenberg, Novel $J_{\text{eff}} = 1/2$ Mott state induced by relativistic spin-orbit coupling in Sr_2IrO_4 , *Phys. Rev. Lett.* **101**, 076402 (2008).
- [5] B. J. Kim, H. Ohsumi, T. Komesu, S. Sakai, T. Morita, H. Takagi, and T. Arima, Phase-sensitive observation of a spin-orbital Mott state in Sr_2IrO_4 , *Science* **323**, 1329 (2009).
- [6] A. Banerjee, C. Bridges, J.-Q. Yan, A. Aczel, L. Li, M. Stone, G. Granroth, M. Lumsden, Y. Yiu, J. Knolle *et al.*, Proximate Kitaev quantum spin liquid behaviour in a honeycomb magnet, *Nat. Mater.* **15**, 733 (2016).
- [7] A. Banerjee, J. Yan, J. Knolle, C. A. Bridges, M. B. Stone, M. D. Lumsden, D. G. Mandrus, D. A. Tennant, R. Moessner, and S. E. Nagler, Neutron scattering in the proximate quantum spin liquid $\alpha\text{-RuCl}_3$, *Science* **356**, 1055 (2017).
- [8] H. Takagi, T. Takayama, G. Jackeli, G. Khaliullin, and S. E. Nagler, Concept and realization of Kitaev quantum spin liquids, *Nat. Rev. Phys.* **1**, 264 (2019).
- [9] Y. Zhang, L.-F. Lin, A. Moreo, and E. Dagotto, Theoretical study of the crystal and electronic properties of $\alpha\text{-RuI}_3$, *Phys. Rev. B* **105**, 085107 (2022).
- [10] S. Vasala and M. Karppinen, $A_2B'B''O_6$ perovskites: A review, *Prog. Solid State Chem.* **43**, 1 (2015).
- [11] S. V. Streltsov and D. I. Khomskii, Orbital physics in transition metal compounds: new trends, *Phys.-Usp.* **60**, 1121 (2017).
- [12] B. Yuan, J. P. Clancy, A. M. Cook, C. M. Thompson, J. Greedan, G. Cao, B. C. Jeon, T. W. Noh, M. H. Upton, D. Casa, T. Gog, A. Paramekanti, and Y.-J. Kim, Determination of Hund's coupling in $5d$ oxides using resonant inelastic x-ray scattering, *Phys. Rev. B* **95**, 235114 (2017).
- [13] F. I. Frontini, C. J. S. Heath, B. Yuan, C. M. Thompson, J. Greedan, A. J. Hauser, F. Y. Yang, M. P. M. Dean, M. H. Upton, D. M. Casa, and Y.-J. Kim, Resonant inelastic X-ray scattering investigation of Hund's and spin-orbit coupling in $5d^2$ double perovskites, [arXiv:2504.20905](https://arxiv.org/abs/2504.20905).
- [14] A. S. Erickson, S. Misra, G. J. Miller, R. R. Gupta, Z. Schlesinger, W. A. Harrison, J. M. Kim, and I. R. Fisher, Ferromagnetism in the Mott insulator $\text{Ba}_2\text{NaOsO}_6$, *Phys. Rev. Lett.* **99**, 016404 (2007).
- [15] C. A. Marjerrison, C. M. Thompson, G. Sala, D. D. Maharaj, E. Kermarrec, Y. Cai, A. M. Hallas, M. N. Wilson, T. J. S. Munsie, G. E. Granroth, R. Flacau, J. E. Greedan, B. D. Gaulin, and G. M. Luke, Cubic Re^{6+} ($5d^1$) double perovskites, $\text{Ba}_2\text{MgReO}_6$, $\text{Ba}_2\text{ZnReO}_6$, and $\text{Ba}_2\text{Y}_{2/3}\text{ReO}_6$: Magnetism, heat capacity, μSR , and neutron scattering studies and comparison with theory, *Inorg. Chem.* **55**, 10701 (2016).
- [16] D. Hirai and Z. Hiroi, Successive symmetry breaking in a $J_{\text{eff}} = 3/2$ quartet in the spin-orbit coupled insulator $\text{Ba}_2\text{MgReO}_6$, *J. Phys. Soc. Jpn.* **88**, 064712 (2019).
- [17] S. Gao, D. Hirai, H. Sagayama, H. Ohsumi, Z. Hiroi, and T. H. Arima, Antiferromagnetic long-range order in the $5d^1$ double-perovskite $\text{Sr}_2\text{MgReO}_6$, *Phys. Rev. B* **101**, 220412(R) (2020).
- [18] D. Hirai, H. Sagayama, S. Gao, H. Ohsumi, G. Chen, T. H. Arima, and Z. Hiroi, Detection of multipolar orders in the spin-orbit-coupled $5d$ Mott insulator $\text{Ba}_2\text{MgReO}_6$, *Phys. Rev. Res.* **2**, 022063(R) (2020).
- [19] I. Živković, J.-R. Soh, O. Malanyuk, R. Yadav, F. Pisani, A. M. Tehrani, D. Tolj, J. Pasztorova, D. Hirai, Y. Wei *et al.*, Dynamic Jahn-Teller effect in the strong spin-orbit coupling regime, *Nat. Commun.* **15**, 8587 (2024).
- [20] D. Hirai, A. Koda, A. Matsuo, K. Kindo, T. Yajima, and Z. Hiroi, Muon spin rotation, high-field magnetization, and structural study on a spin-orbit-entangled Mott insulator $\text{Ba}_2\text{MgReO}_6$, *JPS Conf. Proc.* **30**, 011143 (2020).
- [21] J.-R. Soh, M. E. Merkel, L. V. Pourovskii, I. Živković, O. Malanyuk, J. Pásztorová, S. Francoal, D. Hirai, A. Urru, D.

- Tolj, D. Fiore Mosca, O. V. Yazyev, N. A. Spaldin, C. Ederer, and H. M. Rønnow, Spectroscopic signatures and origin of hidden order in $\text{Ba}_2\text{MgReO}_6$, *Nat. Commun.* **15**, 10383 (2024).
- [22] F. I. Frontini, G. H. J. Johnstone, N. Iwahara, P. Bhattacharyya, N. A. Bogdanov, L. Hozoi, M. H. Upton, D. M. Casa, D. Hirai, and Y.-J. Kim, Spin-orbit-lattice entangled state in A_2MgReO_6 ($\text{A}=\text{Ca}, \text{Sr}, \text{Ba}$) revealed by resonant inelastic x-ray scattering, *Phys. Rev. Lett.* **133**, 036501 (2024).
- [23] H. Arima, Y. Oshita, D. Hirai, Z. Hiroi, and K. Matsubayashi, Interplay between quadrupolar and magnetic interactions in $5d^1$ double perovskite $\text{Ba}_2\text{MgReO}_6$ under pressure, *J. Phys. Soc. Jpn.* **91**, 013702 (2022).
- [24] H. Ishikawa, D. Hirai, A. Ikeda, M. Gen, T. Yajima, A. Matsuo, Y. H. Matsuda, Z. Hiroi, and K. Kindo, Phase transition in the $5d^1$ double perovskite $\text{Ba}_2\text{CaReO}_6$ induced by high magnetic field, *Phys. Rev. B* **104**, 174422 (2021).
- [25] D. Hirai and Z. Hiroi, Possible quadrupole order in tetragonal $\text{Ba}_2\text{CdReO}_6$ and chemical trend in the ground states of $5d^1$ double perovskites, *J. Phys.: Condens. Matter* **33**, 135603 (2021).
- [26] A. E. Taylor, S. Calder, R. Morrow, H. L. Feng, M. H. Upton, M. D. Lumsden, K. Yamaura, P. M. Woodward, and A. D. Christianson, Spin-orbit coupling controlled $J = 3/2$ electronic ground state in $5d^3$ oxides, *Phys. Rev. Lett.* **118**, 207202 (2017).
- [27] A. E. Taylor, R. Morrow, R. S. Fishman, S. Calder, A. I. Kolesnikov, M. D. Lumsden, P. M. Woodward, and A. D. Christianson, Spin-orbit coupling controlled ground state in $\text{Sr}_2\text{ScOsO}_6$, *Phys. Rev. B* **93**, 220408(R) (2016).
- [28] E. Kermarrec, C. A. Marjerrison, C. M. Thompson, D. D. Maharaj, K. Levin, S. Kroecker, G. E. Granroth, R. Flacau, Z. Yamani, J. E. Greedan, and B. D. Gaulin, Frustrated fcc antiferromagnet Ba_2YO_6 : Structural characterization, magnetic properties, and neutron scattering studies, *Phys. Rev. B* **91**, 075133 (2015).
- [29] D. D. Maharaj, G. Sala, C. A. Marjerrison, M. B. Stone, J. E. Greedan, and B. D. Gaulin, Spin gaps in the ordered states of La_2LiXO_6 ($X = \text{Ru}, \text{Os}$) and their relation to the distortion of the cubic double perovskite structure in $4d^3$ and $5d^3$ magnets, *Phys. Rev. B* **98**, 104434 (2018).
- [30] L. V. Pourovskii, Multipolar interactions and magnetic excitation gap in d^3 spin-orbit Mott insulators, *Phys. Rev. B* **108**, 054436 (2023).
- [31] G. Chen and L. Balents, Spin-orbit coupling in d^2 ordered double perovskites, *Phys. Rev. B* **84**, 094420 (2011).
- [32] D. D. Maharaj, G. Sala, M. B. Stone, E. Kermarrec, C. Ritter, F. Fauth, C. A. Marjerrison, J. E. Greedan, A. Paramakanti, and B. D. Gaulin, Octupolar versus Néel order in cubic $5d^2$ double perovskites, *Phys. Rev. Lett.* **124**, 087206 (2020).
- [33] A. Paramakanti, D. D. Maharaj, and B. D. Gaulin, Octupolar order in d -orbital Mott insulators, *Phys. Rev. B* **101**, 054439 (2020).
- [34] S. Voleti, D. D. Maharaj, B. D. Gaulin, G. Luke, and A. Paramakanti, Multipolar magnetism in d -orbital systems: Crystal field levels, octupolar order, and orbital loop currents, *Phys. Rev. B* **101**, 155118 (2020).
- [35] P. Santini, S. Carretta, G. Amoretti, R. Caciuffo, N. Magnani, and G. H. Lander, Multipolar interactions in f -electron systems: The paradigm of actinide dioxides, *Rev. Mod. Phys.* **81**, 807 (2009).
- [36] T. Hotta, Orbital ordering phenomena in d - and f -electron systems, *Rep. Prog. Phys.* **69**, 2061 (2006).
- [37] N. Iwahara, V. Vieru, and L. F. Chibotaru, Spin-orbital-lattice entangled states in cubic d^1 double perovskites, *Phys. Rev. B* **98**, 075138 (2018).
- [38] N. Iwahara and L. F. Chibotaru, Vibronic order and emergent magnetism in cubic d^1 double perovskites, *Phys. Rev. B* **107**, L220404 (2023).
- [39] D. Fiore Mosca, C. Franchini, and L. V. Pourovskii, Interplay of superexchange and vibronic effects in the hidden order of $\text{Ba}_2\text{MgReO}_6$ from first principles, *Phys. Rev. B* **110**, L201101 (2024).
- [40] G. Chen, R. Pereira, and L. Balents, Exotic phases induced by strong spin-orbit coupling in ordered double perovskites, *Phys. Rev. B* **82**, 174440 (2010).
- [41] C. Svoboda, W. Zhang, M. Randeria, and N. Trivedi, Orbital order drives magnetic order in $5d^1$ and $5d^2$ double perovskite Mott insulators, *Phys. Rev. B* **104**, 024437 (2021).
- [42] S. W. Lovesey and D. D. Khalyavin, Lone octupole and bulk magnetism in osmate $5d^2$ double perovskites, *Phys. Rev. B* **102**, 064407 (2020).
- [43] D. Churchill and H.-Y. Kee, Competing multipolar orders in a face-centered cubic lattice: Application to the osmium double perovskites, *Phys. Rev. B* **105**, 014438 (2022).
- [44] L. V. Pourovskii, D. F. Mosca, and C. Franchini, Ferrooctupolar order and low-energy excitations in d^2 double perovskites of osmium, *Phys. Rev. Lett.* **127**, 237201 (2021).
- [45] S. Banerjee, S. Humeniuk, A. R. Bishop, A. Saxena, and A. V. Balatsky, Multipolar multiferroics in $4d^2/5d^2$ Mott insulators, *Phys. Rev. B* **111**, L201107 (2025).
- [46] G. Khalullin, D. Churchill, P. P. Stavropoulos, and H.-Y. Kee, Exchange interactions, Jahn-Teller coupling, and multipole orders in pseudospin one-half $5d^2$ Mott insulators, *Phys. Rev. Res.* **3**, 033163 (2021).
- [47] K. Pradhan, A. Paramakanti, and T. Saha-Dasgupta, Multipolar magnetism in $5d^2$ vacancy-ordered halide double perovskites, *Phys. Rev. B* **109**, 184416 (2024).
- [48] S. Kozłowski, D. Churchill, and H.-Y. Kee, Emergence of quadrupolar order under magnetic field in $5d^2$ double perovskites, *Phys. Rev. B* **111**, 155138 (2025).
- [49] A. Rayyan, X. Liu, and H.-Y. Kee, Fate of multipolar physics in $5d^2$ double perovskites, *Phys. Rev. B* **108**, 045149 (2023).
- [50] R. Morrow, A. E. Taylor, D. J. Singh, J. Xiong, S. Rodan, A. U. B. Wolter, S. Wurmehl, B. Büchner, M. B. Stone, A. I. Kolesnikov, A. A. Aczel, A. D. Christianson, and P. M. Woodward, Spin-orbit coupling control of anisotropy, ground state and frustration in $5d^2\text{Sr}_2\text{MgOsO}_6$, *Sci. Rep.* **6**, 32462 (2016).
- [51] J. Xiong, J. Yan, A. A. Aczel, and P. M. Woodward, Type I antiferromagnetic order in $\text{Ba}_2\text{LuReO}_6$: Exploring the role of structural distortions in double perovskites containing $5d^2$ ions, *J. Solid State Chem.* **258**, 762 (2018).
- [52] G. J. Nilsen, C. M. Thompson, C. Marjerrison, D. I. Badrtdinov, A. A. Tsirlin, and J. E. Greedan, Magnetic order and multipoles in the $5d^2$ rhenium double perovskite Ba_2YReO_6 , *Phys. Rev. B* **103**, 104430 (2021).
- [53] C. M. Thompson, J. P. Carlo, R. Flacau, T. Aharen, I. A. Leahy, J. R. Pollicemi, T. J. S. Munsie, T. Medina, G. M. Luke, J. Munevar, S. Cheung, T. Goko, Y. J. Uemura, and J. E. Greedan, Long-range magnetic order in the $5d^2$ double perovskite $\text{Ba}_2\text{CaOsO}_6$: Comparison with spin-disordered Ba_2YReO_6 , *J. Phys.: Condens. Matter* **26**, 306003 (2014).

- [54] T. Aharen, J. E. Greedan, C. A. Bridges, A. A. Aczel, J. Rodriguez, G. MacDougall, G. M. Luke, V. K. Michaelis, S. Kroecker, C. R. Wiebe, H. Zhou, and L. M. D. Cranswick, Structure and magnetic properties of the $S = 1$ geometrically frustrated double perovskites $\text{La}_2\text{LiReO}_6$ and Ba_2YReO_6 , *Phys. Rev. B* **81**, 064436 (2010).
- [55] A. W. Sleight, J. Longo, and R. Ward, Compounds of osmium and rhenium with the ordered perovskite structure, *Inorg. Chem.* **1**, 245 (1962).
- [56] Y. Sasaki, Y. Doi, and Y. Hinatsu, Magnetic and calorimetric studies of double perovskites $\text{Ba}_2\text{LnReO}_6$ ($\text{Ln} = \text{Y}, \text{Nd}, \text{Sm-Lu}$), *J. Mater. Chem.* **12**, 2361 (2002).
- [57] A. Huq, M. Kirkham, P. F. Peterson, J. P. Hodges, P. S. Whitfield, K. Page, T. Hugle, E. B. Iverson, A. Parizzi, and G. Rennich, POWGEN: Rebuild of a third-generation powder diffractometer at the spallation neutron source, *J. Appl. Crystallogr.* **52**, 1189 (2019).
- [58] O. Arnold, J. Bilheux, J. Borreguero, A. Buts, S. Campbell, L. Chapon, M. Doucet, N. Draper, R. F. Leal, M. Gigg *et al.*, Mantid—Data analysis and visualization package for neutron scattering and μSR experiments, *Nucl. Instrum. Methods Phys. Res. Sect. A* **764**, 156 (2014).
- [59] G. E. Granroth, A. I. Kolesnikov, T. E. Sherline, J. P. Clancy, K. A. Ross, J. P. C. Ruff, B. D. Gaulin, and S. E. Nagler, SEQUOIA: A newly operating chopper spectrometer at the SNS, *J. Phys.: Conf. Ser.* **251**, 012058 (2010).
- [60] R. T. Azuah, L. R. Kneller, Y. Qiu, P. L. Tregenna-Piggott, C. M. Brown, J. R. Copley, and R. M. Dimeo, DAVE: A comprehensive software suite for the reduction, visualization, and analysis of low energy neutron spectroscopic data, *J. Res. Natl. Inst. Stand. Technol.* **114**, 341 (2009).
- [61] G. Kresse and J. Hafner, *Ab initio* molecular dynamics for liquid metals, *Phys. Rev. B* **47**, 558 (1993).
- [62] G. Kresse and J. Furthmüller, Efficient iterative schemes for *ab initio* total-energy calculations using a plane-wave basis set, *Phys. Rev. B* **54**, 11169 (1996).
- [63] P. E. Blöchl, Projector augmented-wave method, *Phys. Rev. B* **50**, 17953 (1994).
- [64] J. P. Perdew, K. Burke, and M. Ernzerhof, Generalized gradient approximation made simple, *Phys. Rev. Lett.* **77**, 3865 (1996).
- [65] S. L. Dudarev, G. A. Botton, S. Y. Savrasov, C. J. Humphreys, and A. P. Sutton, Electron-energy-loss spectra and the structural stability of nickel oxide: An LSDA+U study, *Phys. Rev. B* **57**, 1505 (1998).
- [66] S. Baroni, P. Giannozzi, and A. Testa, Green's-function approach to linear response in solids, *Phys. Rev. Lett.* **58**, 1861 (1987).
- [67] X. Gonze, Perturbation expansion of variational principles at arbitrary order, *Phys. Rev. A* **52**, 1086 (1995).
- [68] L. Chaput, A. Togo, I. Tanaka, and G. Hug, Phonon-phonon interactions in transition metals, *Phys. Rev. B* **84**, 094302 (2011).
- [69] A. Togo and I. Tanaka, First principles phonon calculations in materials science, *Scr. Mater.* **108**, 1 (2015).
- [70] Y. Q. Cheng, L. L. Daemen, A. I. Kolesnikov, and A. J. Ramirez-Cuesta, Simulation of inelastic neutron scattering spectra using OCLIMAX, *J. Chem. Theory Comput.* **15**, 1974 (2019).
- [71] J. Jensen and A. R. Mackintosh, *Rare Earth Magnetism: Structures and Excitations* (Oxford University Press, Oxford, 1991).
- [72] M. Rotter, M. D. Le, A. T. Boothroyd, and J. A. Blanco, Dynamical matrix diagonalization for the calculation of dispersive excitations, *J. Phys.: Condens. Matter* **24**, 213201 (2012).
- [73] A. T. Boothroyd, *Principles of Neutron Scattering from Condensed Matter* (Oxford University Press, Oxford, 2020).
- [74] M. T. Anderson, K. B. Greenwood, G. A. Taylor, and K. R. Poeppelmeier, B-cation arrangements in double perovskites, *Prog. Solid State Chem.* **22**, 197 (1993).
- [75] M. E. Fisher, Relation between the specific heat and susceptibility of an antiferromagnet, *Philos. Mag.* **7**, 1731 (1962).
- [76] K. Kobayashi, T. Nagao, and M. Ito, Radial integrals for the magnetic form factor of $5d$ transition elements, *Acta Cryst. A* **67**, 473 (2011).
- [77] A. Paramekanti, D. J. Singh, B. Yuan, D. Casa, A. Said, Y.-J. Kim, and A. D. Christianson, Spin-orbit coupled systems in the atomic limit: rhenates, osmates, iridates, *Phys. Rev. B* **97**, 235119 (2018).
- [78] D. A. Kukusta, L. V. Bekenov, and V. N. Antonov, Resonant inelastic x-ray scattering in double perovskites from first-principles. I. A_2YReO_6 ($\text{A} = \text{Ba}$ and Sr), *J. Magn. Magn. Mater.* **614**, 172714 (2025).
- [79] S. W. Lovesey, D. D. Khalyavin, G. van der Laan, and G. J. Nilsen, Diffraction by multipoles in a $5d^2$ rhenium double perovskite, *Phys. Rev. B* **103**, 104429 (2021).
- [80] S. Carretta, P. Santini, R. Caciuffo, and G. Amoretti, Quadrupolar waves in uranium dioxide, *Phys. Rev. Lett.* **105**, 167201 (2010).
- [81] R. Caciuffo, P. Santini, S. Carretta, G. Amoretti, A. Hiess, N. Magnani, L.-P. Regnault, and G. H. Lander, Multipolar, magnetic, and vibrational lattice dynamics in the low-temperature phase of uranium dioxide, *Phys. Rev. B* **84**, 104409 (2011).
- [82] L. V. Pourovskii and S. Khmelevskiy, Hidden order and multipolar exchange striction in a correlated f -electron system, *Proc. Natl. Acad. Sci. USA* **118**, e2025317118 (2021).
- [83] <https://doi.org/10.14461/oncat.data/2571601>.